

# A comparison of the Colton–Kirsch inverse scattering methods with linearized tomographic inverse scattering

Michael Brandfass<sup>1</sup>, Aaron D Lanterman<sup>2</sup> and Karl F Warnick<sup>3</sup>

<sup>1</sup> Aero-Sensing Radarsysteme GmbH, Münchner Strasse 20, D-82234 Wessling, Germany

<sup>2</sup> School of Electrical and Computer Engineering, Georgia Institute of Technology, Mail code 0250, Atlanta, GA 30318, USA

<sup>3</sup> Department of Electrical and Computer Engineering, Brigham Young University, 459 Clyde Building, Provo, UT 84602, USA

E-mail: michael.brandfass@aerosensing.de, lanterma@ece.gatech.edu and warnick@byu.edu

Received 1 March 2001, in final form 12 July 2001

Published 15 November 2001

Online at [stacks.iop.org/IP/17/1797](http://stacks.iop.org/IP/17/1797)

## Abstract

We present a numerical comparison of the so-called ‘linear sampling’ inverse scattering methods developed by Colton and Kirsch, published in this journal, and linearized tomographic inverse scattering algorithms based on either holographic filtered backpropagation principles or a plain matrix inversion scheme. Although we restrict ourselves to two-dimensional obstacle scattering, we investigate both the transverse magnetic (TM) and the transverse electric (TE) polarization modes. The comparison of the TM-polarization mode is performed with a specific filtered backpropagation algorithm derived here whereas the comparison of the TE-polarization mode is performed with a matrix inversion scheme. Both suggested schemes, with which we compare the linear sampling method, make use of linearizing approximations whereas the linear sampling method does not introduce any such approximations.

Numerical examples are given for a monofrequent plane wave excitation in angular diversity mode with either full or limited aperture data. In these particular experiments, the linearized tomographic methods appear to provide clearer visual results than the linear sampling methods.

## 1. Introduction

Inverse scattering algorithms have generally fallen into two broad categories: fast, approximate linear algorithms (often based on fast Fourier transforms) or slow, accurate nonlinear algorithms. The linear algorithms often amount to simply inverting a Fourier transform. By contrast, nonlinear algorithms, such as the distorted Born iterative method [1–4], usually require some sort of computationally expensive Newton-like search. Historically, there have

been few options available between these two extremes. Recently, the so-called ‘linear sampling’ method was developed by Colton and Kirsch [5]. (Several of their colleagues, such as Monk, Piana and Potthast, have also made significant contributions.) On one hand, it does not employ any linearizing approximations, but on the other hand, it also does not have to use expensive search techniques to iteratively approach a solution. This new method represents an alternative to the usual extremes in inverse scattering. A recent survey of the various Colton–Kirsch methods as well as other developments in scattering theory is given in [6]. To our knowledge, this paper presents the first comparisons of these methods with linearized tomography algorithms.

Although some extensive derivations underlie Colton and Kirsch’s method, the resulting algorithm is simple. In the original method [5], for each point  $\mathbf{R}$  in the desired image, one solves a linear equation  $\mathbf{F}\mathbf{g} = \mathbf{f}(\mathbf{R})$  for  $\mathbf{g}$ , where  $\mathbf{f}(\mathbf{R})$  is a vector of complex exponentials which depends on the position of the point  $\mathbf{R}$  in the reconstruction and  $\mathbf{F}$  is a matrix formed from the measured data. The theory dictates that the norm of  $\mathbf{g}$  becomes large at the border of the scatterer. Hence, to visualize the scatterer surface, one can simply plot an image of the norms of the  $\mathbf{g}$ s. Since the measurements  $\mathbf{F}$  are typically noisy, the method has been extended [7] to incorporate regularization via Morozov’s discrepancy principle. This principle allows for the fact that the uncertainty lies in the operator  $\mathbf{F}$ , instead of the right-hand side  $\mathbf{f}$  (as is typical in most applications). We will refer to this method as CK-LS (for Colton–Kirsch ‘linear sampling’). Note that although the algorithm involves solving sets of linear equations, it represents a nonlinear kind of processing since it is ultimately the norm of the  $\mathbf{g}$  that is considered. As mentioned, it does not assume any linearizing approximations (such as the Born or Kirchhoff approximations which underly most linear reconstruction algorithms).

One appealing aspect of the method is that no *a priori* knowledge of the boundary condition is needed. As shown in [5, 8], the exact same prescription holds for Dirichlet, Neumann or impedance boundary conditions. It is also helpful in cases where the scatterer is a penetrable, inhomogeneous medium; in these situations, the method gives the support of the scatterer. The method has hence been helpful in biomedical applications, such as detecting leukemia [9–11].

Kirsch [12, 13] derived a variation on the method which involves solving  $(\mathbf{F}^*\mathbf{F})^{1/4}\mathbf{g} = \mathbf{f}(\mathbf{R})$  at each point, and again looking for points where  $\|\mathbf{g}\|$  blows up. The theory for homogeneous and inhomogeneous media and given in [12] and [13], respectively. We will refer to this method as K-MLS (for Kirsch ‘modified linear sampling’). When convenient, both CK-LS and K-MLS will be referred to generically as the ‘Colton–Kirsch methods’<sup>4</sup>.

### 1.1. Theory versus practice

Although the underlying theory of the Colton–Kirsch methods is extensive, and a few numerical examples are given in the papers cited above, comparatively little is known about the precise behaviour of the algorithm in practice.

For the original Colton–Kirsch method, i.e. CK-LS (using  $\mathbf{F}\mathbf{g} = \mathbf{f}$ ), the available theorems say that  $\|\mathbf{g}(\mathbf{R})\| \rightarrow \infty$  as  $\mathbf{R}$  approaches the boundary from *inside* the scatterer, in the sense that if we solve  $\mathbf{F}\mathbf{g} = \mathbf{f}$  with discrepancy  $\epsilon$  (measured with squared-error norm), it is known that  $\|\mathbf{g}_\epsilon(\mathbf{R})\| \rightarrow \infty$  as  $\epsilon \rightarrow 0$ . Although, in practice,  $\|\mathbf{g}(\mathbf{R})\|$  is also observed to blow up for  $\mathbf{R}$  *outside* the scatterer, there is no theory at present to explain why. The lack of such a theorem led Kirsch to propose the K-MLS method (using  $(\mathbf{F}^*\mathbf{F})^{1/4}\mathbf{g} = \mathbf{f}$ ); in this case, the theory shows that  $\|\mathbf{g}(\mathbf{R})\|$  should be infinite outside the scatterer.

<sup>4</sup> Most papers by the inventors of these methods refer to them using the term ‘linear sampling’. We attach the developers’ names in order to try to avoid confusion with the many other possible interpretations of the words ‘linear sampling’. This will be especially important as these techniques infiltrate the mainstream electrical engineering literature, where ‘linear’ and ‘sampling’ have all sorts of meanings.

The application of regularization to the methods is somewhat unique, in that one usually applies regularization to *avoid* extremely large estimates arising from ill-conditioning, whereas here large  $\|g(\mathbf{R})\|$  are the main object of interest. Plots of  $\|g(\mathbf{R})\|$  show a wide variety of structure inside the scatterer. Unfortunately, the theorems give no insight into the behaviour of  $\|g(\mathbf{R})\|$  away from the boundary inside the scatterer.

The Colton–Kirsch methods are fundamentally single-frequency methods, with no obvious way to combine information from illuminations with different frequencies. This contrasts with linearized tomography methods, which naturally combine information from different frequencies. Also, in these linear inversion methods, it is easy to predict the performance degradation with limited data, since it involves simple blurring by the point-spread function associated with that aperture. The original basic formulation of the Colton–Kirsch theorems, however, all assume that a full aperture (a complete set of incident and observation angles) is available. A reviewer pointed out that the theory of CK-LS is easily extended to the limited aperture case; quoting the reviewer directly, ‘the change in the ill-posedness is due to the change of approximation quality of a point-source by a Herglotz wavefunction with limited aperture’, as discussed in the theorems of Ochs [14, 15]. The same reviewer noted that the extension of K-MLS is not nearly as straightforward; a recent such advancement is established in [16].

### 1.2. Scope and organization

Most of the work on Colton–Kirsch methods has been in two dimensions. The scatterer is assumed to be an infinitely long cylinder whose profile does not change along the  $z$ -dimension. In the acoustic case, one can then deal with the two-dimensional Helmholtz equation. In the electromagnetic case, if the field is polarized so that the electric or magnetic field runs parallel to the axis of the scatterer, Maxwell’s equations reduce to the two-dimensional Helmholtz equation. Although the method has been extended to the three-dimensional scalar (acoustic) case [17] and the three-dimensional vector (electromagnetic) case [18], our exposition will focus on two-dimensional problems.

Section 2 reviews the details of the Colton–Kirsch reconstruction methods, and section 3.1 describes a linearized tomographic imaging algorithm for transverse magnetic (TM) polarization, which was derived from [19, 20] and based on the fundamentals given in [21]. In section 3.2, a very simple linearized reconstruction scheme is given for the transverse electric (TE) polarization case. Section 4 compares reconstructions for simulated data using both the Colton–Kirsch and the linearized inversion algorithms. Suggestions for further investigation are offered in section 5.

## 2. Details of the Colton–Kirsch methods

Let  $\hat{\mathbf{R}}'$  denote the unit vector pointed in the direction of an observation point and  $\hat{\mathbf{k}}_i$  denote the direction unit vector of an incident plane wave with wavenumber  $k = 2\pi f/c = \omega/c$ . In what follows, non-bold italic versions of otherwise bold-faced vectors represent the radial component (i.e. distance from the origin) of the vector.

### 2.1. Fundamentals

Denote the measured bistatic far-field pattern as  $u_\infty(\hat{\mathbf{R}}', \hat{\mathbf{k}}_i)$ . Consider the linear operator given by

$$\int_{\Omega} u_{\infty}(\hat{\mathbf{R}}', \hat{\mathbf{k}}_i) g(\hat{\mathbf{k}}_i, \mathbf{R}) ds(\hat{\mathbf{k}}_i) = \frac{e^{j\frac{\pi}{4}}}{\sqrt{8\pi k}} e^{-jk\hat{\mathbf{R}}' \cdot \mathbf{R}}, \quad \hat{\mathbf{R}}' \in \Omega. \quad (1)$$

This is called the far-field equation in [5, 7].  $\Omega$  is the unit circle and  $ds$  is the measure on the unit circle. CK-LS is based on the observation that the solution  $g$  of (1) has norm which goes to infinity as  $\mathbf{R}$  approaches the boundary of the scatterer from inside. It can be shown that  $g(\hat{\mathbf{k}}_i, \mathbf{R})$  satisfies equation (1) only if there exists a solution of a certain boundary value problem for which this solution is a so-called Herglotz wavefunction of specific form. However, such a solution can only be found for a few scatterer geometries (e.g. a circular cylinder). Because of this reason, equation (1) is solved in the least-square sense incorporating a penalty term to alleviate the ill-posedness of equation (1). The reader is referred to [5, 7] for further details.

For numerical implementation, discretize (1) as

$$\mathbf{F}g = \mathbf{f}(\mathbf{R}), \quad (2)$$

where

$$\mathbf{F} = \begin{bmatrix} u_{\infty}(\hat{\mathbf{R}}'_1, \hat{\mathbf{k}}_{i;1}) & u_{\infty}(\hat{\mathbf{R}}'_1, \hat{\mathbf{k}}_{i;2}) & \cdots & u_{\infty}(\hat{\mathbf{R}}'_1, \hat{\mathbf{k}}_{i;N}) \\ u_{\infty}(\hat{\mathbf{R}}'_2, \hat{\mathbf{k}}_{i;1}) & u_{\infty}(\hat{\mathbf{R}}'_2, \hat{\mathbf{k}}_{i;2}) & \cdots & u_{\infty}(\hat{\mathbf{R}}'_2, \hat{\mathbf{k}}_{i;N}) \\ \vdots & \vdots & \ddots & \vdots \\ u_{\infty}(\hat{\mathbf{R}}'_N, \hat{\mathbf{k}}_{i;1}) & u_{\infty}(\hat{\mathbf{R}}'_N, \hat{\mathbf{k}}_{i;2}) & \cdots & u_{\infty}(\hat{\mathbf{R}}'_N, \hat{\mathbf{k}}_{i;N}) \end{bmatrix}, \quad (3)$$

$$\mathbf{g}(\mathbf{R}) = [g(\hat{\mathbf{k}}_{i;1}, \mathbf{R}), g(\hat{\mathbf{k}}_{i;2}, \mathbf{R}) \cdots g(\hat{\mathbf{k}}_{i;N}, \mathbf{R})]^T, \quad (4)$$

and

$$\mathbf{f}_n(\mathbf{R}) = \frac{e^{j\frac{\pi}{4}}}{\sqrt{8\pi k}} e^{-jk\hat{\mathbf{R}}'_n \cdot \mathbf{R}}. \quad (5)$$

For CK-LS, equation (2) must be solved for a large number of  $\mathbf{R}$  to form an image. For K-MLS, we solve  $(\mathbf{F}^* \mathbf{F})^{1/4} g = \mathbf{f}(\mathbf{R})$  instead.

One can computationally simplify matters by exploiting a singular value decomposition (SVD) of  $\mathbf{F}$  [7, 12]. Denote the SVD of the far-field operator as  $\mathbf{F} = \mathbf{U} \mathbf{S} \mathbf{V}^H$ . Let  $\boldsymbol{\rho} = \mathbf{U}^H \mathbf{f}$  and  $\boldsymbol{\mu} = \mathbf{V}^H \mathbf{f}$ . The needed norm for CK-LS is given by

$$\|\mathbf{g}\|^2 = \sum_{n=1}^N \frac{|\rho_n|^2}{s_n^2}. \quad (6)$$

For K-MLS, it is given by

$$\|\mathbf{g}\|^2 = \sum_{n=1}^N \frac{|\mu_n|^2}{s_n}. \quad (7)$$

## 2.2. Regularization via Morozov's discrepancy principle

Incorporating regularization via Morozov's discrepancy principle involves simple modifications [7, 12] of (6) and (7). To specify the regularization, suppose that the distance between the available noisy data  $\mathbf{F}$  and the true far-field  $\mathbf{F}_{\text{true}}$ , as measured by the Frobenius norm (square root of the sum of the squares of the elements), is bounded by  $\delta$ , i.e.  $\|\mathbf{F} - \mathbf{F}_{\text{true}}\| \leq \delta$ . Here we simply state the results; see [6] or [17] for details of the formulation.

For the CK-LS method, the norm for the regularized problem is given by

$$\|\mathbf{g}\|^2 = \sum_{n=1}^N \frac{s_n^2}{(\alpha + s_n^2)^2} |\rho_n|^2, \quad (8)$$

where  $\alpha$  is the zero of

$$m_A(\alpha) = \sum_{n=1}^N \frac{\delta^2 s_n^2 - \alpha^2}{(\alpha + s_n^2)^2} |\rho_n|^2. \tag{9}$$

For K-MLS, it is given by

$$\|g\|^2 = \sum_{n=1}^N \frac{s_n}{(\alpha + s_n)^2} |\mu_n|^2, \tag{10}$$

where  $\alpha$  is the zero of

$$m_B(\alpha) = \sum_{n=1}^N \frac{\delta^2 s_n - \alpha^2}{(\alpha + s_n)^2} |\mu_n|^2. \tag{11}$$

In most image processing applications, regularization enforces some kind of correlation between neighbouring pixels. This is not the case here; the regularization is applied independently in finding  $g$  for each particular point  $R$ .

### 3. Linearized tomographic inverse scattering methods

#### 3.1. Reconstruction of TM-polarized scattered field data

The approach used for the linearized TM-polarization reconstructions is based on holographic backpropagation principles [19–21]. A derivation of the scalar angular diversity algorithm in Fourier domain according to equation (32) can be found in [21]. However, no derivation from Fourier space back to the spatial domain was provided there. The scheme, derived in this paper, has the advantage that data do not have to be mapped to a two-dimensional Fourier space, interpolated to a rectangular Fourier coordinate system and finally transformed to the reconstruction domain via an inverse two-dimensional Fourier transform, as in usual diffraction tomography algorithms. In [19] an extension from scalar to vector electromagnetic tomography is presented for frequency and angular diversity algorithms in bistatic and monostatic set-ups making use of the holographic backpropagation principle. A small note of the scalar version of the angular diversity formula (34) can also be found in [19]. In [20] a Fourier domain vector electromagnetic angular diversity algorithm is presented, which makes use of a vector holographic field representation.

In the following, we derive a formula which connects the far-field data on the measurement surface to the reconstruction domain directly via holographic backpropagation principles. The scalar representation of the holographic field is given by

$$\Theta_H(\mathbf{R}, \omega) = - \int_{\partial S} \left[ E_s(\mathbf{R}', \hat{\mathbf{k}}_i, \omega) \frac{\partial G^*(\mathbf{R} - \mathbf{R}', \omega)}{\partial n'} - G^*(\mathbf{R} - \mathbf{R}', \omega) \frac{\partial E_s(\mathbf{R}', \hat{\mathbf{k}}_i, \omega)}{\partial n'} \right] ds(\mathbf{R}') \tag{12}$$

$$= -2kZ \int_S J_c(\mathbf{R}', \hat{\mathbf{k}}_i, \omega) G_i(\mathbf{R} - \mathbf{R}', \omega) d^2 \mathbf{R}' \tag{13}$$

$$= e^{j\frac{\pi}{4}} \sqrt{\frac{k}{2\pi}} \int_{\Omega} u_{\infty}(\hat{\mathbf{R}}', \hat{\mathbf{k}}_i, \omega) e^{jk\mathbf{R} \cdot \hat{\mathbf{R}}'} ds(\hat{\mathbf{R}}') \tag{14}$$

where  $\partial S$  and  $S$  is the surface of the scatterer and the full scatterer domain, respectively. The far-field pattern is given by

$$u_\infty(\hat{\mathbf{R}}', \hat{\mathbf{k}}_i, \omega) = Z \sqrt{\frac{k}{8\pi}} e^{-j\frac{\pi}{4}} \int_S J_c(\mathbf{R}', \hat{\mathbf{k}}_i, \omega) e^{-jk\hat{\mathbf{R}} \cdot \mathbf{R}'} d^2 \mathbf{R}' \quad (15)$$

with the scattered electric field  $E_s(\mathbf{R}, \hat{\mathbf{k}}_i, \omega)$  polarized in the direction of the infinite scatterer cylinder axis.  $G_i(\mathbf{R} - \mathbf{R}', \omega)$  is the imaginary part of the scalar Green function of the Helmholtz equation in free space and  $G^*(\mathbf{R} - \mathbf{R}', \omega)$  is the conjugate scalar Green function, according to

$$G_i(\mathbf{R} - \mathbf{R}', \omega) = \frac{1}{4} J_0(k|\mathbf{R} - \mathbf{R}'|), \quad (16)$$

$$G^*(\mathbf{R} - \mathbf{R}', \omega) = -\frac{j}{4} H_0^{(2)}(k|\mathbf{R} - \mathbf{R}'|), \quad (17)$$

where  $J_0(x)$  and  $H_0^{(2)}(x)$  are the Bessel function of zeroth order and the Hankel function of the second kind and zeroth order, respectively. The free space wave impedance is denoted as  $Z$ . Applying the Green theorem, we are able to express the holographic field as an integral over the secondary equivalent sources, which are given by

$$jkZJ_c(\mathbf{R}, \hat{\mathbf{k}}_i, \omega) = -k^2 O(\mathbf{R}) E(\mathbf{R}, \hat{\mathbf{k}}_i, \omega), \quad (18)$$

to obtain equation (13).  $J_c(\mathbf{R}, \hat{\mathbf{k}}_i, \omega)$  as defined via equation (18) is the current density of the scatterer domain induced by the total electric field  $E(\mathbf{R}, \hat{\mathbf{k}}_i, \omega)$ , which in turn is a superposition of the incident and the scattered electric field  $E_s(\mathbf{R}, \hat{\mathbf{k}}_i, \omega)$ . According to [22, 23] such integral methods have been introduced by Esmarch as early as 1913. However, they were first applied to holographic fields by Porter and Bojarski [24, 25] and extended to the vector electromagnetic case in [19, 26].  $O(\mathbf{R})$  is the object function, which is the reconstruction quantity we are looking for. It can also be shown that the holographic field can be expressed through an integration of the far-field pattern times a phase term over the unit circle  $\Omega$ , according to equation (14). Note that (13) and (18), taken together, corresponds to equation (8.27) of [27].

In two-dimensional angular diversity, the incident plane wave angle  $\vartheta_i$  varies in the interval  $[0, 2\pi]$ . We have to choose a coordinate system which rotates in sync with the rotation of the incident plane wave excitation, i.e. one coordinate axis has to point in the direction of the incident field direction of the plane wave. We decompose the Fourier-space vector  $\mathbf{K}$  and reconstruction domain vector  $\mathbf{R}$  in their components with respect to the rotating coordinate system as shown in figure 1, which is expressed by equations (21) and (22), respectively:

$$\hat{\mathbf{k}}_i = \cos \vartheta_i \mathbf{e}_z + \sin \vartheta_i \mathbf{e}_x, \quad (19)$$

$$\mathbf{K} = \underbrace{K \sin \vartheta_K \mathbf{e}_x + K \cos \vartheta_K \mathbf{e}_z}_{=K\mathbf{e}_r} \quad (20)$$

$$= K_{\parallel} \hat{\mathbf{k}}_i + K_{\perp} \hat{\mathbf{k}}_{i\perp} \quad (21)$$

$$\mathbf{R} = R_{\parallel} \hat{\mathbf{k}}_i + R_{\perp} \hat{\mathbf{k}}_{i\perp}. \quad (22)$$

Let  $F(\omega)$  denote the frequency spectrum of the incident plane wave. Introducing the Born approximation into equation (18), which basically neglects the scattered field within the scatterer, and choosing a plane wave as the incident field so that we have for the total field  $E(\mathbf{R}, \hat{\mathbf{k}}_i, \omega) = E_i(\mathbf{R}, \hat{\mathbf{k}}_i, \omega) = F(\omega) e^{jk\hat{\mathbf{k}}_i \cdot \mathbf{R}}$ , and substituting the Born approximated

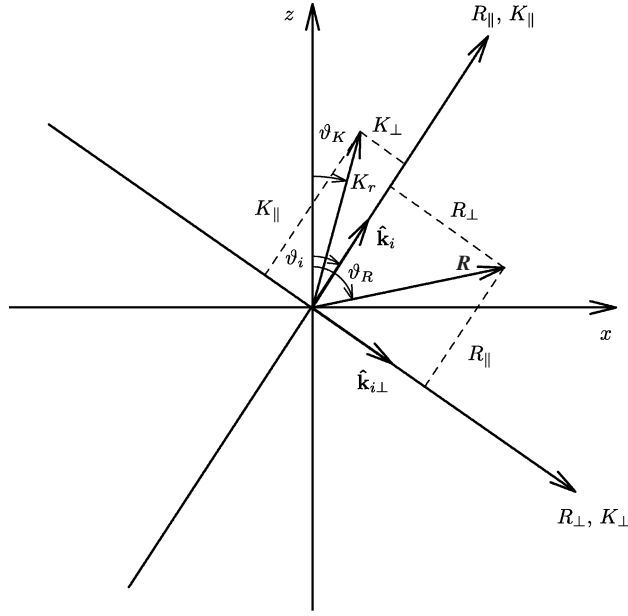


**Figure 1.** Definition of the coordinate system in angular diversity mode.

equation (18) into (13), we obtain, after subsequent a two-dimensional Fourier transform with respect to  $\mathbf{R}$ ,

$$\tilde{\Theta}_H(\mathbf{K} + k\hat{\mathbf{k}}_i, \omega) = -j2k^2 F(\omega) \tilde{O}(\mathbf{K}) \tilde{G}_i(\mathbf{K} + k\hat{\mathbf{k}}_i, \omega) \quad (23)$$

$$= -j2\pi k^2 F(\omega) \text{sign}(k) \tilde{O}(\mathbf{K}) \delta(K^2 + 2k\hat{\mathbf{k}}_i \cdot \mathbf{K}) \quad (24)$$

where tildes denote Fourier transformed quantities. The imaginary part of the two-dimensional free-space Green function in  $\mathbf{K}$ -space is given by<sup>5</sup>

$$\tilde{G}_i(\mathbf{K}, \omega) = \pi \text{sign}(k) \delta(K^2 - k^2). \quad (25)$$

Although the examples in this paper only deal with single-frequency excitation, for which  $F(\omega)$  is just a complex number, we keep the  $\omega$ -dependency in our derivations for greatest generality. With the generalized sifting theorem of  $\delta$ -distributions according to

$$\delta(f(x)) = \sum_{j=1}^n \frac{\delta(x - x_j)}{f'(x_j)} \quad (26)$$

we can compute the integration of the  $\delta$ -distributions over the incident angles so that for

$$\int_{\Omega} \delta(K^2 + 2k\hat{\mathbf{k}}_i \cdot \mathbf{k}) ds(\hat{\mathbf{k}}_i) = 2 \int_{\vartheta_K}^{\pi + \vartheta_K} \underbrace{\delta(K^2 + 2kK \cos(\vartheta_i - \vartheta_K))}_{=f(\vartheta_i)} d\vartheta_i \quad (27)$$

with

$$\cos(\vartheta_{ij} - \vartheta_K) = -\frac{K}{2k}, \quad (28)$$

$$f'(\vartheta_{ij}) = -2kK \sin(\vartheta_{ij} - \vartheta_K), \quad (29)$$

<sup>5</sup> Equation (25) holds for two as well as for three dimensions in  $\mathbf{K}$ -space, though of course, the Green functions for two and three dimensions are different in  $\mathbf{R}$ -space [19].

it follows that

$$\delta(f(\vartheta_i)) = \frac{\delta(\vartheta_i - \vartheta_{i1})}{2K| - k \sin(\vartheta_{i1} - \vartheta_K)|} u(k) + \frac{\delta(\vartheta_i - \vartheta_{i2})}{2K| - k \sin(\vartheta_{i2} - \vartheta_K)|} u(-k) \quad (30)$$

where  $u(k)$  is the unit-step function, cutting off either the positive or conjugate negative part of the frequency spectrum. Making use of equations (27)–(29), we finally obtain, for the integration over the incident angles,

$$\int_{\Omega} \delta(K^2 + 2k\hat{\mathbf{k}}_i \cdot \mathbf{K}) ds(\hat{\mathbf{k}}_i) = \frac{1}{|k| \sqrt{K^2 - \frac{K^4}{4k^2}}} u(2|k| - K), \quad (31)$$

so that the object function in the Fourier space reads

$$\tilde{O}(\mathbf{K}) u(2|k| - K) = \frac{j}{4\pi k F(\omega)} \int_{\Omega} \sqrt{K^2 - \frac{K^4}{4k^2}} \tilde{\Theta}_H(\mathbf{K} + k\hat{\mathbf{k}}_i, \omega) ds(\hat{\mathbf{k}}_i). \quad (32)$$

As indicated through equation (24) the holographic field in Fourier space  $\tilde{\Theta}_H(\mathbf{K} + k\hat{\mathbf{k}}_i, \omega)$  has  $\delta$ -distributive character. Therefore, we are able to simplify the square-root expression under the integral of equation (32) applying the sifting theorem in a reverse direction making use of equation (28) so that it follows:

$$\tilde{O}(\mathbf{K}) u(2|k| - K) = \frac{j}{4\pi k F(\omega)} \int_{\Omega} |\hat{\mathbf{k}}_{i\perp} \cdot \mathbf{K}| \tilde{\Theta}_H(\mathbf{K} + k\hat{\mathbf{k}}_i, \omega) ds(\hat{\mathbf{k}}_i). \quad (33)$$

Hence, with the inverse two-dimensional Fourier transform we obtain

$$O^{\text{bl}}(\mathbf{R}) = \frac{j}{2\pi^2 k F(\omega)} \int_{\Omega} \hat{\mathbf{k}}_{i\perp} \cdot \nabla [\Theta_H(\mathbf{R}, \omega) e^{-jk\hat{\mathbf{k}}_i \cdot \mathbf{R}}] ds(\hat{\mathbf{k}}_i) *_{1D} \text{pf} \left( \frac{1}{\hat{\mathbf{k}}_{i\perp} \cdot \mathbf{R}} \right) \quad (34)$$

where pf is the abbreviation for *pseudofunction* and  $O^{\text{bl}}(\mathbf{R})$  in equation (34) denotes a band-limited version of  $O(\mathbf{R})$  as a result of the unit-step function  $u(2|k| - K)$  which in turn is introduced by equation (30). The one-dimensional convolution  $*_{1D}$  has to be performed with respect to the  $R_{\perp}$ -component of the  $\mathbf{R}$ -vector. With the substitution of

$$E_s^{\text{far}}(\mathbf{R}, \hat{\mathbf{k}}_i, \omega) = \frac{e^{jkR}}{\sqrt{R}} u_{\infty}(\hat{\mathbf{R}}, \hat{\mathbf{k}}_i, \omega) \quad (35)$$

into equation (14) and the resulting holographic field formula in equation (34) we are able to solve the one-dimensional convolution in equation (34) in accordance with

$$e^{jkR \cdot (\hat{\mathbf{R}}' - \hat{\mathbf{k}}_i)} *_{1D} \text{pf} \left( \frac{1}{\hat{\mathbf{k}}_{i\perp} \cdot \mathbf{R}} \right) = e^{jkR \cdot (\hat{\mathbf{R}}' - \hat{\mathbf{k}}_i)} \underbrace{\int_{-\infty}^{+\infty} e^{-jk\tilde{R}_{\perp} \hat{\mathbf{k}}_{i\perp} \cdot \hat{\mathbf{R}}'} \frac{1}{\tilde{R}_{\perp}} d\tilde{R}_{\perp}}_{=-j\pi \text{sign}(k\hat{\mathbf{k}}_{i\perp} \cdot \hat{\mathbf{R}}')} \quad (36)$$

The final result for the object function in the reconstruction domain is a simple two-fold integral over the observation-point angular and incident-field angular unit circle:

$$O^{\text{bl}}(\mathbf{R}) = \frac{1}{4\sqrt{\pi^3}} \text{Re} \left\{ \frac{\sqrt{|k|}}{F(\omega)} \int_{\Omega} \int_{\Omega} E_s^{\text{far}}(\mathbf{R}', \hat{\mathbf{k}}_i, \omega) \sqrt{R'} e^{-jkR'} \right. \\ \left. \times e^{jkR \cdot (\hat{\mathbf{R}}' - \hat{\mathbf{k}}_i)} |\hat{\mathbf{k}}_{i\perp} \cdot \hat{\mathbf{R}}'| ds(\hat{\mathbf{R}}') ds(\hat{\mathbf{k}}_i) \right\}. \quad (37)$$

The numerical evaluation of this formula is very easy. Discretized in equidistant angles, it can basically be computed by just one matrix–vector and one subsequent vector–vector

multiplication for each reconstruction point. No regularization is necessary since equation (37) belongs to the class of generalized filtered backpropagation algorithms, where in this special case, equation (37) has already been analytically inverse Fourier transformed to the reconstruction domain.

We have seen from equation (25) that the two-dimensional Fourier transform of the imaginary part of the free space Green function corresponds to a  $\delta$ -distribution in  $\mathbf{K}$ -space which is singular on non-concentric circles varying in orientation and size with direction and frequency of the incident wave, respectively. Because of the sifting property of the  $\delta$ -distribution only those parts of the Fourier transformed equivalent secondary sources in equation (24) are considered for which it becomes singular. All other areas outside these circles are set to zero leading to a unique mapping rule between scattered field data and object function. Hence, the information from the equivalent secondary sources available by this filtering procedure is just its minimal energy contribution. Therefore, such linearized holographic field filtered backpropagation algorithms are well posed and always lead to stable and unique solutions [28–30].

### 3.2. Reconstruction of TE-polarized scattered field data

We use a different reconstruction approach for the TE-polarization, which, after introduction of a linearizing approximation, invokes a simple matrix inversion to retrieve the singular function vector components  $\gamma_x$  and  $\gamma_y$  of the scatterer. It basically represents the first linearized stage of a numerical nonlinear inversion approach presented in [31], for which a more sophisticated regularization scheme was introduced as well as a multilevel multipole algorithm to speed up the iteration process. However, due to the iterative nature of that algorithm it is considerably slower than the algorithm presented here.

For the perfect electric conductor case with a conductivity  $\sigma \rightarrow \infty$ , the object function  $O(\mathbf{R})$  can be described as a two-dimensional unit-step function, according to

$$\Gamma(\mathbf{R}) = \begin{cases} 1 & \text{for } \mathbf{R} \in S \\ 0 & \text{else } \mathbf{R} \notin S. \end{cases} \quad (38)$$

This unit-step function is equal to zero outside the two-dimensional scatterer domain  $S$  and equal to unity inside. Such a unit-step function can be defined by a potential function  $\Phi(\mathbf{R})$  so that

$$\Gamma(\mathbf{R}) = u(\Phi(\mathbf{R})) \quad \text{with} \quad \Phi(\mathbf{R}) \begin{cases} < 0 & \text{for } \mathbf{R} \notin S \cup \partial S \\ = 0 & \text{for } \mathbf{R} \in \partial S \\ > 0 & \text{for } \mathbf{R} \in S. \end{cases} \quad (39)$$

Applying the gradient on the two-dimensional unit-step function as defined in equation (39) we can introduce a vector singular function  $\gamma(\mathbf{R})$  as the reconstruction quantity for the TE-case [32], yielding

$$\gamma(\mathbf{R}) = -\nabla\Gamma(\mathbf{R}) = \delta(\Phi(\mathbf{R})) \nabla\Phi(\mathbf{R}) = \delta(\Phi(\mathbf{R})) |\nabla\Phi(\mathbf{R})| \mathbf{n} = \gamma(\mathbf{R}) \mathbf{n}. \quad (40)$$

The unit normal of the scatterer is directed outwards according to  $\mathbf{n} = \nabla\Phi(\mathbf{R})/|\nabla\Phi(\mathbf{R})|$ . The secondary equivalent current sources can now be expressed through the definitions in equation (40) so that

$$\mathbf{J}_c(\mathbf{R}, \omega) = \gamma(\mathbf{R}) \mathbf{J}_s(\mathbf{R}, \omega) = -\mathbf{n}(\mathbf{R}) \cdot \nabla\Gamma(\mathbf{R}) \mathbf{J}_s(\mathbf{R}, \omega). \quad (41)$$

We can see from this equation that the secondary equivalent current density  $\mathbf{J}_c(\mathbf{R}, \omega)$  is singular on the contour of the scatterer and equal to zero everywhere else because of the sifting property

of the vector singular function as defined in equation (40).  $\mathbf{J}_s(\mathbf{R}, \omega)$  is the surface current density and can be considered as the weight of the vector singular function.

The magnetic field on the measurement surface is an integral equation of the first kind, expressed in terms of the equivalent current density defined through equation (41). The integral kernel  $G(\mathbf{R}, \mathbf{R}', \omega)$  is given by the free space scalar Green function for two dimensions. Its complex conjugate is provided by equation (17). Since we restrict ourselves to two dimensions, the magnetic field  $H_z^{sM}(\mathbf{R}, \omega)$  has only one component in direction of the axis of the cylindrical scatterer:

$$H_z^{sM}(\mathbf{R}, \omega) = e_z \cdot \int_{S_R} [\nabla' \times \mathbf{J}_c(\mathbf{R}', \omega)] G(\mathbf{R}, \mathbf{R}', \omega) d^2 \mathbf{R}'. \quad (42)$$

$S_R$  is the reconstruction domain which fully encloses the scatterer domain  $S \cup \partial S$ .  $\mathbf{R}$  is the observation point on the measurement surface. Inserting the second boundary condition for perfectly conducting surfaces according to

$$\left. \begin{aligned} \mathbf{n} \times \mathbf{E}(\mathbf{R}, \omega) &= 0 \\ \mathbf{n} \times \mathbf{H}(\mathbf{R}, \omega) &= \mathbf{J}_s(\mathbf{R}, \omega) \end{aligned} \right\}, \quad \text{for } \mathbf{R} \in \partial S \text{ and } \sigma \rightarrow \infty \quad (43)$$

into equation (41), and in turn inserting equation (41) into the integral equation for the magnetic field  $H_z^{sM}(\mathbf{R}, \omega)$  according to equation (42) and considering the fact that the scatterer's surface normal  $\mathbf{n}(\mathbf{R})$  is perpendicular to the cylindrical scatterer axis  $e_z$ , we obtain (after introduction of the Kirchhoff approximation  $H_z(\mathbf{R}, \omega) = 2 H_z^i(\mathbf{R}, \omega)|_{\mathbf{R} \in \partial S}$ ) the linearized integral equation of the scattered magnetic field on the measurement surface which can be stated as

$$H_z^{sM}(\mathbf{R}, \omega) = -2 \int_{S_R} H_z^i(\mathbf{R}', \omega) \gamma(\mathbf{R}') \cdot \nabla' G(\mathbf{R}, \mathbf{R}', \omega) d^2 \mathbf{R}'. \quad (44)$$

Note by introduction of the Kirchhoff approximation we have simply replaced the total magnetic field  $H_z(\mathbf{R}, \omega)$  in the integral by the incident magnetic field  $H_z^i(\mathbf{R}, \omega)$  on the contour of the scatterer, making use of the sifting theorem of the vector singular function  $\gamma(\mathbf{R})$  in equation (44). Performing an integration by parts on equation (44) and making use of Gauss' theorem, we find the scattered magnetic field according to

$$H_z^{sM}(\mathbf{R}, \omega) = 2 \int_{\partial S} H_z^i(\mathbf{R}', \omega) \mathbf{n}' \cdot \nabla' G(\mathbf{R}, \mathbf{R}', \omega) ds(\mathbf{R}') \quad (45)$$

where  $\partial S$  is the contour of the scatterer. Note through the introduction of the vector singular function  $\gamma(\mathbf{R})$  we observe that the contour integral formula in equation (45) is identical to the formulation in equation (44).

The vector singular function  $\gamma(\mathbf{R})$  is the reconstruction quantity we are looking for in the TE-case for a perfectly conducting scatterer, so we choose equation (44) to discretize the reconstruction domain. Via the method of moments with use of pulse-basis functions and point matching, we end up with the following matrix equation:

$$\mathbf{H}_s^{[M \times 1]} = \overline{\mathbf{G}}^{[M \times 2L]} \overline{\boldsymbol{\gamma}}^{[2L \times L]} \mathbf{H}_i^{[L \times 1]} \quad (46)$$

$$= \underbrace{\overline{\mathbf{G}}^{[M \times 2L]} \overline{\mathbf{H}}_i^{[2L \times 2L]}}_{\overline{\mathbf{C}}^{[M \times 2L]}} \boldsymbol{\gamma}^{[2L \times 1]}, \quad (47)$$

with the matrices  $\overline{\mathbf{G}}$ ,  $\overline{\mathbf{H}}_i$  and  $\overline{\boldsymbol{\gamma}}$  as well as the vector  $\boldsymbol{\gamma}$  according to

$$\overline{\mathbf{H}}_i^{[2L \times 2L]} = \left[ \begin{array}{c|c} \mathcal{D}\{\overline{\mathbf{H}}_i^{[L \times 1]}\} & \overline{\mathbf{0}} \\ \hline \overline{\mathbf{0}} & \mathcal{D}\{\overline{\mathbf{H}}_i^{[L \times 1]}\} \end{array} \right], \quad (48)$$

$$\overline{\gamma}^{[2L \times L]} = \begin{bmatrix} \overline{\gamma}_x^{[L \times L]} \\ \overline{\gamma}_y^{[L \times L]} \end{bmatrix}, \quad \gamma^{[2L \times 1]} = \begin{bmatrix} \gamma_x^{[L \times 1]} \\ \gamma_y^{[L \times 1]} \end{bmatrix}. \quad (49)$$

The operator  $\mathcal{D}$  creates a diagonal matrix whose diagonal entries are given by the vector operated on.  $\overline{\mathbf{H}}_i$  consists of two submatrices which are diagonal and both the same. The Green matrix and the singular function element matrix of equations (46) and (47) are structured as

$$\overline{\mathbf{G}}^{[L \times 2L]} = \begin{bmatrix} g_1^x(\mathbf{r}_1) & \cdots & g_1^x(\mathbf{R}_L) & | & g_1^y(\mathbf{R}_1) & \cdots & g_1^y(\mathbf{R}_L) \\ \vdots & \ddots & \vdots & | & \vdots & \ddots & \vdots \\ g_L^x(\mathbf{R}_1) & \cdots & g_L^x(\mathbf{R}_L) & | & g_L^y(\mathbf{R}_1) & \cdots & g_L^y(\mathbf{R}_L) \end{bmatrix}, \quad (50)$$

$$\overline{\gamma}^{[2L \times L]} = \begin{bmatrix} \gamma_1^x(\mathbf{R}_1) & \cdots & 0 \\ \vdots & \ddots & \vdots \\ 0 & \cdots & \gamma_L^x(\mathbf{R}_L) \\ \hline \gamma_1^y(\mathbf{R}_1) & \cdots & 0 \\ \vdots & \ddots & \vdots \\ 0 & \cdots & \gamma_L^y(\mathbf{R}_L) \end{bmatrix}. \quad (51)$$

The discretized total magnetic field vector and the singular function element vector are given by

$$\mathbf{H}_i^{[L \times 1]} = [H_z^i(\mathbf{R}_1), H_z^i(\mathbf{R}_2), \dots, H_z^i(\mathbf{R}_v), \dots, H_z^i(\mathbf{R}_L)]^T, \quad (52)$$

$$\gamma^{[2L \times 1]} = [\gamma^x(\mathbf{R}_1), \dots, \gamma^x(\mathbf{R}_v), \dots, \gamma^x(\mathbf{R}_L), \gamma^y(\mathbf{R}_1), \dots, \gamma^y(\mathbf{R}_v), \dots, \gamma^y(\mathbf{R}_L)]^T. \quad (53)$$

The observation point vector is denoted as  $\mathbf{R}_v$ .

Because of the ill-posedness of equation (47) we have to consider multiple incident angles and regularization. For simplicity, we choose Tikhonov regularization with  $\lambda$  as the regularization parameter. Since the reconstruction quantity  $\gamma$  is real, we can split up the matrix  $\overline{\mathbf{C}}^{[M \times 2L]}$  and the left-hand side of equation (47) into its real and imaginary parts and order the submatrices and left-hand sides for the different incident angle experiments according to

$$\overline{\mathbf{A}}^{[2MN \times 2L]} = [\text{Re}\{\overline{\mathbf{C}}_1\}^T, \text{Im}\{\overline{\mathbf{C}}_1\}^T, \dots, \text{Re}\{\overline{\mathbf{C}}_N\}^T, \text{Im}\{\overline{\mathbf{C}}_N\}^T, \sqrt{\lambda} \overline{\mathbf{I}}]^T \quad (54)$$

$$\mathbf{b}^{[2MN \times 1]} = [\text{Re}\{\mathbf{H}_{s;1}\}^T, \text{Im}\{\mathbf{H}_{s;1}\}^T, \dots, \text{Re}\{\mathbf{H}_{s;N}\}^T, \text{Im}\{\mathbf{H}_{s;N}\}^T, \mathbf{0}]^T \quad (55)$$

so that we have

$$\overline{\mathbf{A}}^{[2MN \times 2L]} \gamma^{[2L \times 1]} - \mathbf{b}^{[2MN \times 1]} = \mathbf{0}. \quad (56)$$

Equation (56) can be solved in a least square sense via a conjugate gradient scheme.

#### 4. Simulations

We simulated scattering data for the airplane shapes shown in figure 2. The shapes are profiles of the VFY-218, the B-2, the F-15 and the YF-23. We remind the reader that we are assuming the objects are infinitely long cylinders with the profiles shown in figure 2, and not the three-dimensional shapes of the original aircraft. The VFY-218, F-15, and YF-23 are approximately 15.5, 19.5 and 20.5 m long, respectively. Although the real B-2 is much larger than the other aircraft, we have artificially scaled our model to make it 15.5 m wide. We computed data at  $f = 100$  and 200 MHz for both TE and TM polarizations, with  $c = 3 \times 10^8$  m s<sup>-1</sup>. Either a full 360° of incident and observation angles were used or a limited aperture with 180°, 120°, or 90° of incident and observation angles were considered, with data computed at three

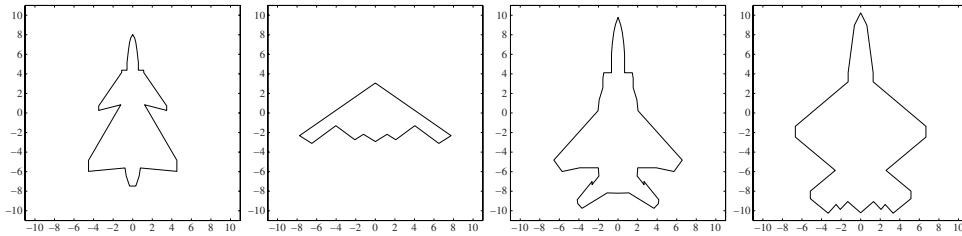


**Figure 2.** Boundaries of two-dimensional objects used in the simulations comparing Colton–Kirsch methods with linear tomographic algorithms. From left to right: VFY-218, B-2, F-15 and YF-23.

degree increments. (Readers interested in conducting their own experiments may contact the second author to obtain MATLAB files containing this simulated scattering data and the precise geometries of the four airplane shapes.)

#### 4.1. Forward solver

The forward scattering data were generated by solving a boundary integral equation on the scatterer surface. The method of moments [33] was used to discretize the integral equation, and the resulting linear system was solved by direct factorization to yield an approximation to the surface current on the object for a given incident field. The far fields radiated by the surface current then give the scattering amplitude as a function of angle. A discretization density of at least ten unknowns per wavelength is employed. Since the scatterers considered are closed bodies, the combined field integral equation formulation was used to ensure accurate results even if the frequency is near an internal resonance of the object.

#### 4.2. Computational results

The images in this section are 200 by 200 pixels, with a spacing of 0.125 m between pixels. We show reconstruction results using both CK-LS and K-MLS. We choose  $\delta = 0.02$ , although we have not explicitly added any noise to the data. The frequency for the plane wave excitation is either  $f = 100$  or 200 MHz. 120 observation points and 120 incident plane waves, which enclose the entire reconstruction domain with an equidistant  $3^\circ$  angular spacing, chosen for both, are used throughout. Figures 3 and 4 show reconstruction results under TM-polarization for excitation frequencies of 100 and 200 MHz, respectively. Figures 5 and 6 present the reconstruction results for the TE-polarization and figure 7 depicts reconstruction results under a limited observation aperture as well as a limited range of incident illumination angles. The left column always shows the reconstruction results from CK-LS, the middle column presents the results from K-MLS, and the right column depicts the reconstructions given by the linearized tomography algorithms. Following the practice in [6, 17], the Colton–Kirsch reconstructions are presented by displaying  $1/\|g(\mathbf{R})\|$  instead of  $\|g(\mathbf{R})\|$ .

By manually adjusting the gray scale from image to image, we sometimes found it possible to subjectively bring out certain features more clearly. (For instance, we empirically found that simply taking the pixelwise square-root of the CK-LS images made them somewhat resemble the K-MLS images.) Since it is difficult to do this adjustment in an objective and consistent way, all images are presented normalized to their own individual maxima.

Although theory predicts that the norm  $\|g(\mathbf{R})\|$  should blow up as  $\mathbf{R}$  approaches the boundary of the scatterer from inside the scatterer, in our experiments, *the outline of the*

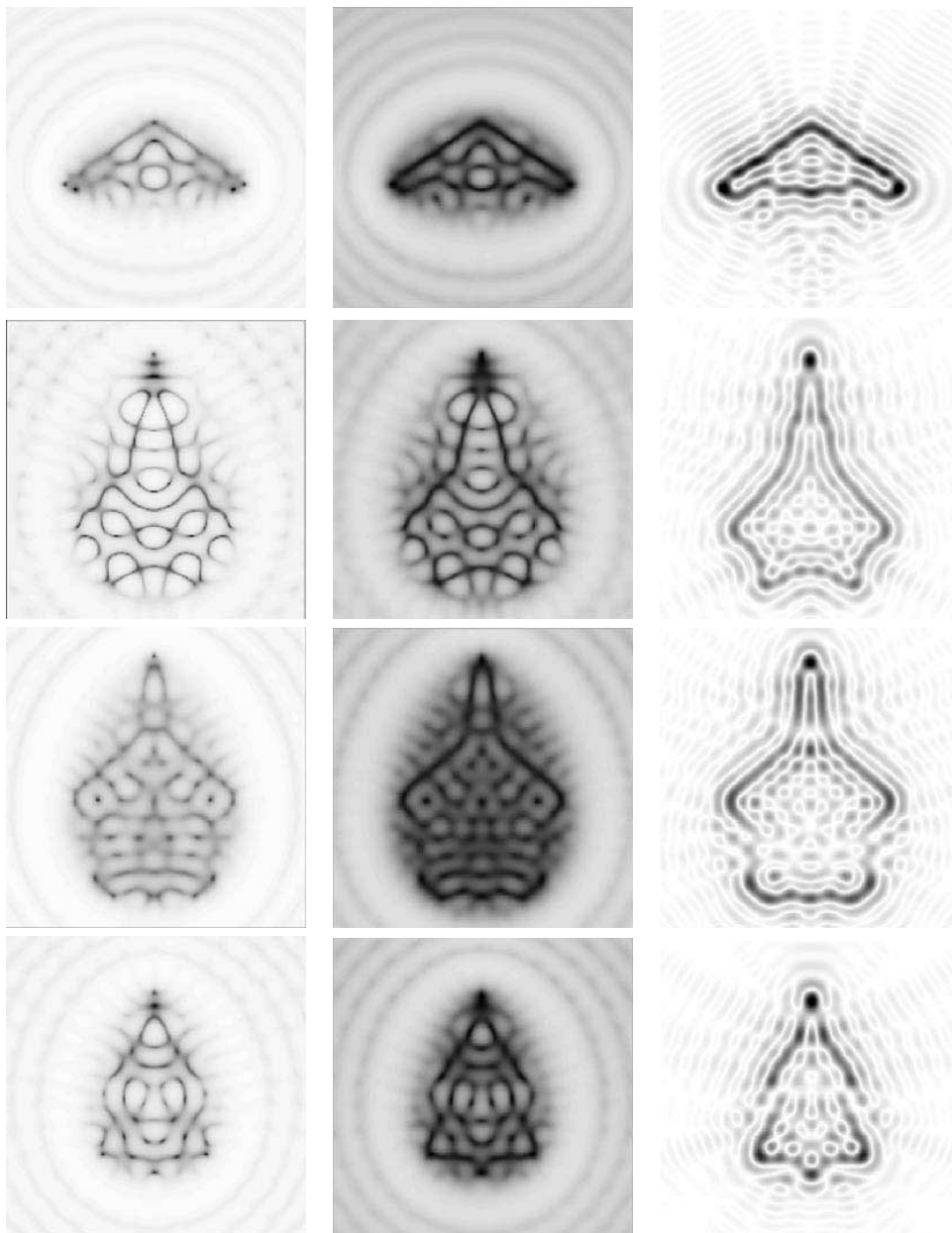


**Figure 3.** Colton–Kirsch methods versus linear inverse scattering reconstruction results for the TM-case, frequency 100 MHz, full aperture. Top to bottom rows: B-2, F-15, YF-23 and VFY-218. Left column: CK-LS method; middle column: K-MLS method; right column: linear inverse scattering method.

*scatterer is most evident where  $\|g(\mathbf{R})\|$  is the least!* The norm seems to blow up at an egg-shaped wrapping around the convex hull of the targets. This seems particularly evident in the K-MLS imagery.

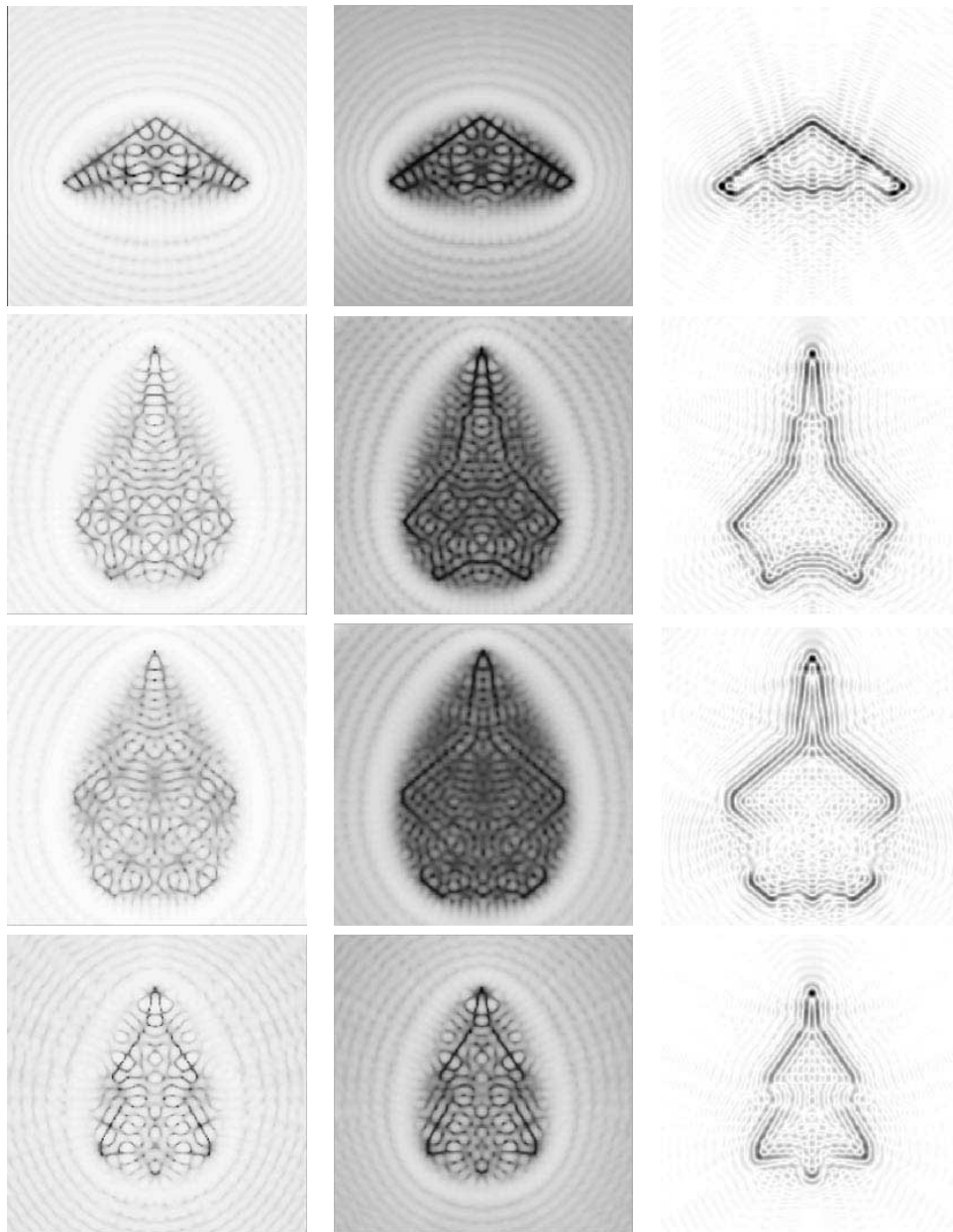


**Figure 4.** Colton–Kirsch method versus linear inverse scattering reconstruction results for the TM-case, frequency 200 MHz, full aperture. Top to bottom rows: B-2, F-15, YF-23 and VFY-218. Left column: CK-LS method; middle column: K-MLS method; right column: linear inverse scattering method.

#### 4.3. Comparison of reconstruction results

We can see from the reconstruction results in figures 3 and 4 that the distortions and artefacts inside and outside the scatterer reconstructions are very strong for both the Colton–Kirsch

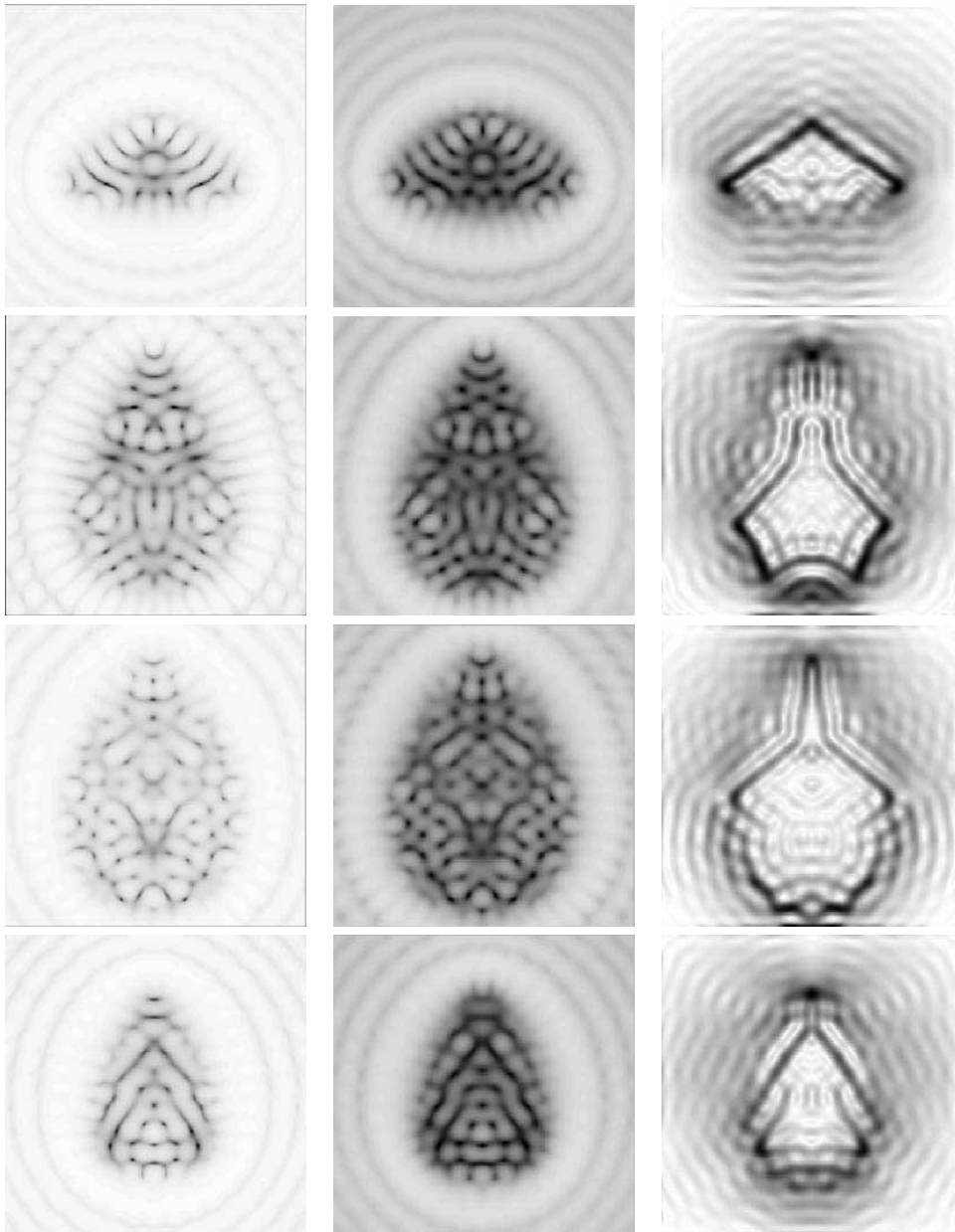


**Figure 5.** Colton–Kirsch method versus linear inverse scattering reconstruction results for the TE-case, frequency 100 MHz, full aperture. Top to bottom rows: B-2, F-15, YF-23 and VFY-218. Left column: CK-LS method; middle column: K-MLS method; right column: linear inverse scattering method.

reconstruction methods in TM-polarization mode. These artificial patterns become denser with higher excitation frequencies. Comparing these results with the results obtained by the TM-polarization linearized tomography reconstruction results, the latter appears qualitatively clearer since the shapes of the scatterers are much more easily distinguished from the artefacts.

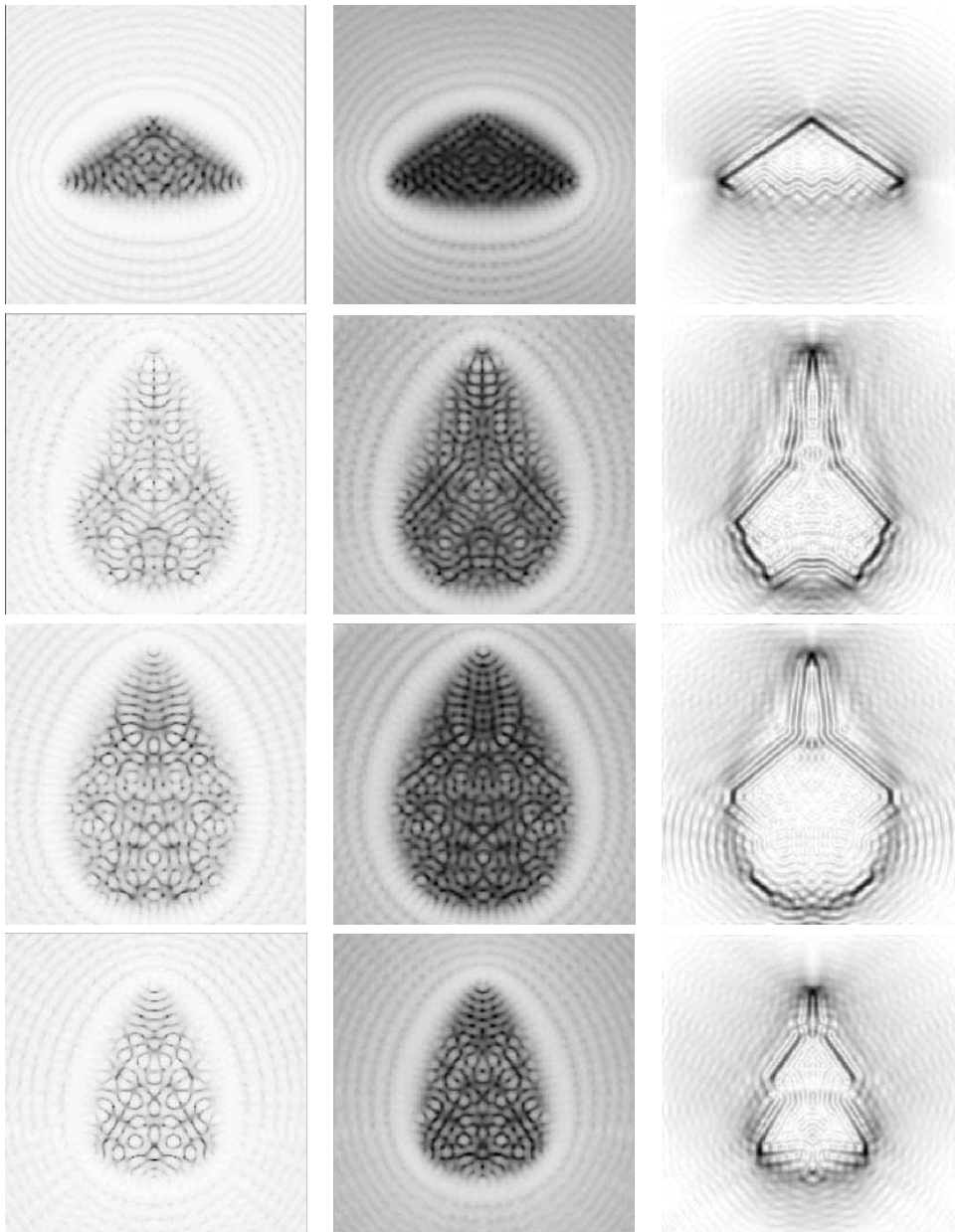


**Figure 6.** Colton–Kirsch method versus linear inverse scattering reconstruction results for the TE-case, frequency 200 MHz, full aperture. Top to bottom rows: B-2, F-15, YF-23 and VFY-218. Left column: CK-LS; middle column: K-MLS method; right column: linear inverse scattering method.

This is especially true for the comparison with CK-LS. We should note, however, that the linear reconstruction schemes assume knowledge of the boundary conditions, whereas the Colton–Kirsch methods do not. Cakoni *et al* [34] show how this makes the Colton–Kirsch methods particularly helpful for partially coated obstacles.

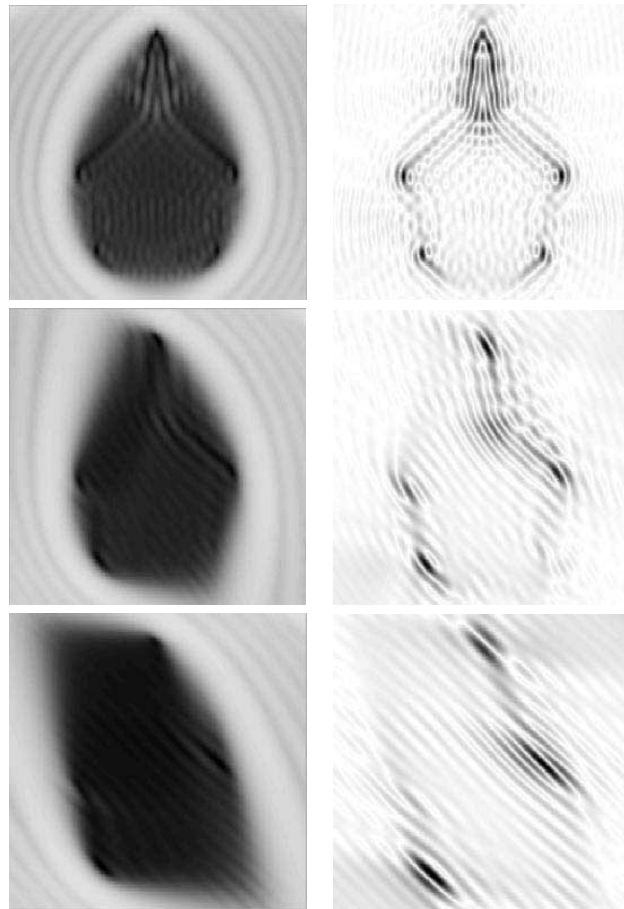


**Figure 7.** K-MLS linear sampling method versus linear inverse scattering reconstruction results for TM-case, frequency 200 MHz, for the YF-23 with a limited aperture. First row: observation aperture  $[0, \pi]$ , incident plane wave angles  $[\pi, 2\pi]$ ; second row: observation aperture  $[0, 2/3\pi]$ , incident plane wave angles  $[\pi, 5/3\pi]$ ; third row: observation aperture  $[0, \pi/2]$ , incident plane wave angles  $[\pi, 3\pi/2]$ ; left column: K-MLS method; right column: linear inverse scattering method.

Since no linearizing approximations are introduced in the development of the Colton–Kirsch methods, we would expect multiple subscatterer interaction effects to be taken into account. In particular, we would expect concave structures of the scatterer shapes to be visible in the Colton–Kirsch reconstructions (but not in the tomographic reconstructions due to the linearizing approximations). However, in practice, the Colton–Kirsch reconstructions do not seem to indicate any features of the scatterer that cannot also be readily observed in the linearized tomography reconstructions. In particular, the Colton–Kirsch reconstructions only seem to show the result of direct reflection effects caused by the incident plane waves.

Taking a close look at the TE-polarization case shown in figures 5 and 6, we see that the corresponding reconstruction results for the Colton–Kirsch methods visually look significantly worse than for the TM-polarization case. The artificial reconstruction patterns become stronger and the true scatterer contour cannot be readily distinguished from these artefacts. However, the simple matrix inversion scheme, as outlined in section 3.2, shows clearer reconstruction results than the Colton–Kirsch methods, though they appear slightly

worse than the reconstruction results obtained through the linearized tomography algorithm under TM-polarization in figures 3 and 4. (One exception is the rear wing structure of the B-2 at 200 MHz, which seems more evident in the Colton–Kirsch reconstructions than in the linear reconstructions.) We conjecture two possible explanations for this behaviour:

- (i) In general, inverse scattering reconstructions for the TM polarization generally appear to be qualitatively better than TE results. One possible explanation for this is the different behaviours of surface waves for the two polarizations. A surface wave current mode radiates fields which travel parallel to the scatterer surface. If the incident wave strikes a scatterer in a direction that is parallel to the surface of the scatterer, the incident wave itself produces a surface wave. But for other incidence angles, surface waves are produced by diffraction from edges and corners of the scatterer, so they result from multiple scattering. For this reason, we might expect strong surface wave components in the surface current on the scatterer to lead to degraded reconstructions for inverse scattering algorithms which are sensitive to multiple scattering. For the TM polarization, surface waves are weak, whereas for the TE polarization, surface waves are stronger. From an operator point of view, the eigenvalues of surface wave modes are large in the TM case [35], so that they are suppressed in the surface current. For the TE polarization, the surface wave eigenvalues are small, so that surface waves tend to have a larger amplitude. Even for convex scatterers with no multiple scattering in the usual sense, in the TE case this type of multiple scattering associated with surface waves is significant relative to single scattering. This may account for the poorer quality of TE reconstructions.
- (ii) Considering the Colton–Kirsch algorithm in particular, as we can see from equation (44), the Green function has to be differentiated with respect to  $\mathbf{R}$ . Instead of the zeroth-order Hankel function which appears in the TM-polarization case, the first-order Hankel function has to be applied for TE-polarization case. From Rellich's lemma in [7] the zeroth-order Hankel function was introduced as the right-hand side of the near-field version of the far-field equation given by equation (1). Although derivations exploiting Huygens' integral representations and Green theorem showed that the far-field equation can be satisfied for some  $g(\mathbf{k}_i, \mathbf{R}')$  for both the TM- and the TE-polarization cases if there exists a solution of a certain boundary value problem, where this solution has to be a Herglotz wavefunction of a specific form [5, 7], the zeroth-order Hankel-function might not adapt to the underlying physics of wave propagation very well in the case of TE-polarization.

Figure 7 depicts the reconstruction results for a limited angular aperture and a limited incident angle variation of the plane wave excitation. The left column shows results of the K-MLS algorithm and the right column shows results of the linearized tomography method. The uppermost row shows basically the same features of the YF-23 cross-section reconstruction for both of the reconstruction algorithms. The results were obtained under a limited observation point aperture of  $[0, \pi]$  and an incident plane wave angle variation of  $[\pi, 2\pi]$ . The row in the middle also reveals the same features of the airplane model. The aperture for the observation angles was  $[0, 2/3\pi]$  and for the incident angles was  $[\pi, 5/3\pi]$ . As expected, the lateral resolution decreases with decreasing aperture angle. The lowermost row shows the reconstruction results for an observation angle aperture of  $[0, \pi/2]$  and an incident wave variation of  $[\pi, 3\pi/2]$ .

After a few minor modifications, both the TM- and TE-polarization tomography algorithms are applicable for projection reconstructions for three-dimensional scatterers even if scattering data is only available along a line or closed circular aperture. The Colton–Kirsch methods, which were not intended for such experimental set-ups, break down under these kinds of scenarios.

## 5. Directions for future work

Our experiments make it clear that much more work needs to be done to understand the consequences of numerically implementing the Colton–Kirsch methods. The fact that the scatterer outline is far more evident where  $\|g\|$  is at a minimum, instead of where it is large as the theory suggests, yearns for further mathematical investigation. The superiority of reconstructions from TM-polarized data to those from TE-polarized is also curious. In the previous section, we conjectured several plausible explanations which may open the door to further analysis. We hope that our experiments will encourage the development of new theory in this area. Further simulation studies, including studies exploring cases where the linear tomographic methods break down more dramatically, and seeing how the Colton–Kirsch methods compare in such cases, could spur further intuition. The analysis of our present results has been admittedly qualitative; in further studies, it would be helpful to develop a more quantitative measure of reconstruction accuracy.

Potthast [36] has proposed the ‘point-source method’, another fast algorithm similar in spirit to Colton and Kirsch’s method. Some related mathematics, and slightly clearer prescription of Potthast’s method, is given in [37]. Kirsch has also crafted a new ‘sampling’ method [16] in which, instead of solving a set of linear equations at each point and looking for where norms blow up, you solve a one-dimensional optimization problem at each point and look for points where a certain quadratic form is nonzero. It would be of interest to compare Potthast’s method and Kirsch’s new method with both the Colton–Kirsch and linearized tomography methods compared above. Furthermore, we are pursuing the numerical investigation of reconstructing airplane projections from three-dimensional airplane models, using only data collected from line apertures, taking the polarization of electromagnetic waves fully into account. The tomographic algorithms to perform these reconstructions can be obtained from [19].

## Acknowledgments

This work was conducted while all three authors were with the University of Illinois at Urbana-Champaign. The authors would like to thank David Colton of the University of Delaware for visiting the University of Illinois at Urbana-Champaign to give a presentation and participate in discussions about linear sampling inverse scattering methods. We would also like to thank him and his colleague Peter Monk for helpful and encouraging comments on the manuscript, and the knowledgeable anonymous reviewers for several detailed observations.

This work was supported by DARPA under Contract F49620-98-1-0498, administered by AFOSR.

## References

- [1] Chew W C and Wang Y M 1990 Reconstruction of two-dimensional permittivity distribution using the distorted Born iterative method *IEEE Trans. Med. Imaging* **9** 218–25
- [2] Joachimowicz N, Pichot C and Hugonin J P 1991 Inverse scattering: an iterative numerical method for electromagnetic imaging *IEEE Trans. Antennas Propag.* **39** 1742–51
- [3] Chiu C-C and Kiang Y-W 1991 Electromagnetic imaging for an imperfectly conducting cylinder *IEEE Trans. Antennas Propag.* **39** 1632–9
- [4] Roger A 1981 Newton–Kantorovitch algorithm applied to an electromagnetic inverse problem *IEEE Trans. Antennas Propag.* **29** 232–8
- [5] Colton D and Kirsch A 1996 A simple method of solving inverse scattering problems in the resonance region *Inverse Problems* **12** 383–93

- [6] Colton D, Coyle J and Monk P 2000 Recent developments in inverse acoustic scattering theory *SIAM Rev.* **42** 369–414
- [7] Colton D, Piana M and Potthast R 1997 A simple method using Morozov's discrepancy principle for solving inverse scattering problems *Inverse Problems* **13** 1477–93
- [8] Colton D and Piana M 1998 The simple method for solving the electromagnetic inverse scattering problem: the case of TE polarized waves *Inverse Problems* **14** 597–614
- [9] Colton D and Monk P 1998 A linear sampling method for the detection of leukemia using microwaves *SIAM J. Appl. Math.* **58** 926–41
- [10] Colton D and Monk P 1994 The detection and monitoring of leukemia using electromagnetic waves: mathematical theory *Inverse Problems* **10** 1235–51
- [11] Colton D and Monk P 1995 The detection and monitoring of leukemia using electromagnetic waves: numerical analysis *Inverse Problems* **11** 329–42
- [12] Kirsch A 1998 Characterization of the shape of a scattering obstacle using the spectral data of the far field operator *Inverse Problems* **14** 1489–512
- [13] Kirsch A 1999 Factorization of the far-field operator for the inhomogeneous medium case and an application to inverse scattering theory *Inverse Problems* **15** 413–29
- [14] Ochs R L 1987 The limited aperture problem of inverse acoustic scattering theory: Dirichlet boundary conditions *SIAM J. Appl. Math.* **47** 1320–1
- [15] Ochs R L 1989 A version of Runge's theorem for the Helmholtz equation with applications to scattering theory *Proc. Edinburgh Math. Soc.* **32** 107–19
- [16] Kirsch A 2000 New characterizations of solutions in inverse scattering theory *Appl. Anal.* **76** 319–50
- [17] Colton D, Giebermann K and Monk P 2000 A regularized sampling method for solving three-dimensional inverse scattering problems *SIAM J. Sci. Comput.* **21** 2316–30
- [18] Colton D, Haddar H and Monk P The linear sampling method for solving the electromagnetic inverse scattering problem *SIAM J. Sci. Comput.* submitted
- [19] Brandfass M 1996 *Inverse Beugungstheorie Elektromagnetischer Wellen: Algorithmen und Numerische Realisierung* (Berlin: Shaker)
- [20] Brandfass M and Langenberg K J 1992 Polarimetric microwave inverse scattering as applied to nondestructive testing *Review of Progress in Quantitative Nondestructive Evaluation* vol 11A, ed D E Chimenti and D O Thompson (New York: Plenum) pp 741–8
- [21] Langenberg K J 1987 Applied inverse problems for acoustic, electromagnetic, and elastic waves *Basic Methods of Tomography and Inverse Problems* ed P C Sabatier (Bristol: Adam Hilger)
- [22] Born M and Wolf E 1980 *Principles of Optics* 6th edn (New York: Pergamon)
- [23] Chew W C 1995 *Waves and Fields in Inhomogeneous Media* (Piscataway, NJ: IEEE)
- [24] Porter R P 1970 Diffraction limited, scalar image formation with holograms of arbitrary shape *J. Opt. Soc. Am.* **60** 1051–9
- [25] Bojarski N N 1982 A survey of the near-field far-field inverse source integral equation *IEEE Trans. Antennas Propag.* **30** 975–9
- [26] Langenberg K J, Brandfass M, Fellingner P, Gurke T and Kreutter T 1994 A unified theory of multidimensional electromagnetic vector inverse scattering within the Kirchhoff or Born approximation *Radar Target Imaging* vol 13, ed W-M Boerner and H Überall (Berlin: Springer) pp 113–51
- [27] Colton D and Kress R 1998 *Inverse Acoustic and Electromagnetic Scattering Theory* 2nd edn (Berlin: Springer)
- [28] Porter R P and Devaney A J 1982 Holography and the inverse source problem *J. Opt. Soc. Am.* **72** 327–30
- [29] Bleistein N and Cohen J K 1977 Nonuniqueness in the inverse source problem in acoustics and electromagnetics *J. Math. Phys.* **18** 194–201
- [30] Dudley D G, Habashy T M and Wolf E 2000 Linear inverse problems in wave motion: non-symmetric first-kind integral equations *IEEE Trans. Antennas Propag.* **48** 1607–17
- [31] Brandfass M and Chew W C 2001 A multilevel fast multipole based approach for efficient reconstruction of perfectly conducting scatterers *J. Electromagn. Waves Appl.* **15** 81–106
- [32] Cohen J K and Bleistein N 1979 The singular function of a surface and physical optics inverse scattering *Wave Motion* **11** 153–61
- [33] Harrington R F 1961 *Time-Harmonic Electromagnetic Fields* (New York: McGraw-Hill)
- [34] Cakoni F, Colton D and Monk P 2001 The direct and inverse scattering problems for partially coated obstacles *Inverse Problems* **17** 1997–2015
- [35] Warnick K F and Chew W C 2001 On the spectrum of the electric field integral equation and the convergence of the moment method *Int. J. Numer. Methods Eng.* **51** 31–56
- [36] Potthast R 1996 A fast new method to solve inverse scattering problems *Inverse Problems* **12** 731–42
- [37] Kress R and Paivarinta L 1999 On the far field in obstacle scattering *SIAM J. Appl. Math.* **59** 1413–26